SCIENCE CHINA
Chemistry

•ARTICLES•
SPECIAL ISSUE: 2025 Emerging Investigator Issue

December 2025 Vol.68 No.12: 6639–6647
https://doi.org/10.1007/s11426-025-2781-4

Modulating pyrene-based covalent organic framework via BF_2 functionalization for facilitated photocatalytic proton-coupled electron-transfer reductions

Zhipeng Luo[1,2†], Xiaowen Chen[1,2†], Wanxiang Yang[1,2†], Yu Chang[3†], Shipeng Zhu[1,2],
Fengtao Zhang[1,2], Wei Lin[1,2*], Gang Xu[3], Guan-E Wang[3*] & Xiong Chen[1,2*]

[1]*State Key Laboratory of Chemistry for NBC Hazards Protection, College of Chemistry, Fuzhou University, Fuzhou 350116, China*
[2]*State Key Laboratory of Photocatalysis on Energy and Environment, and Key Laboratory of Advanced Carbon-Based Functional Materials, College of Chemistry, Fuzhou University, Fuzhou 350116, China*
[3]*State Key Laboratory of Structural Chemistry, Fujian Provincial Key Laboratory of Materials and Techniques toward Hydrogen Energy, Fujian Institute of Research on the Structure of Matter, Chinese Academy of Sciences, Fuzhou 350002, China*

Received March 18, 2025; accepted May 19, 2025; published online July 21, 2025

The investigation of charge carrier kinetics has long been a cornerstone of polymer photocatalysis research. However, the role of proton transport behavior in photocatalytic processes has often been underappreciated, despite its fundamental importance in proton-coupled electron-transfer reactions. Addressing this gap, we present a novel BF_2-bridged covalent organic framework (C2-COF-BF2) that undergoes post-synthetic modification with boron trifluoride, designed to confer a dual functional advantage. Specifically, the incorporated BF_2 moieties are engineered to induce a donor-acceptor effect and potentially serve as continuous supply sites for activated protons. This bifunctional role not only enhances charge separation and migration while suppressing electron-hole recombination but also facilitates proton transport, thereby enabling improved performance in both photocatalytic hydrogen evolution reaction (HER) and H_2O_2 production. Remarkably, the photocatalytic HER performance of C2-COF-BF2 ($AQY_{450\ nm}$ = 8.78%) ranks among the highest efficiencies reported for COF-based photocatalysts to date. These findings highlight an innovative pathway for advancing the rational design of COF photocatalysts, offering a synergistic optimization of charge carrier kinetics and mass transfer processes to achieve unprecedented photocatalytic efficiency.

covalent organic frameworks, BF_2 functionalization, photocatalytic proton-coupled electron-transfer reductions, charge separation and migration, proton transport

Citation: Luo Z, Chen X, Yang W, Chang Y, Zhu S, Zhang F, Lin W, Xu G, Wang GE, Chen X. Modulating pyrene-based covalent organic framework via BF_2 functionalization for facilitated photocatalytic proton-coupled electron-transfer reductions. *Sci China Chem*, 2025, 68: 6639–6647, https://doi.org/10.1007/s11426-025-2781-4

1 Introduction

The urgent transition from conventional fossil fuels to sustainable energy sources is imperative for ensuring the long-term viability of modern human society. Among renewable energy options, solar energy stands out as an abundant and virtually inexhaustible resource with immense potential to meet the escalating global energy demands [1,2]. Efficiently harnessing solar energy through its conversion into chemical energy, particularly in the form of green hydrogen—the "holy grail" of sustainable energy—offers a transformative strategy to address global energy scarcity [3]. This pursuit has driven extensive research into the development of advanced photocatalysts for various reactions such as water

---

†Equally contributed to this work.
*Corresponding authors (email: wlin@fzu.edu.cn; gewang@fjirsm.ac.cn; chenxiong987@fzu.edu.cn, chenxiong987@iccas.ac.cn)

splitting and H_2O_2 production, with significant strides made in polymeric systems, including polymeric carbon nitride [4–8], conjugated microporous polymers [9–13], linear polymers [14–17], and covalent organic frameworks (COFs) [18–22], *etc*.

COFs, distinguished by their crystalline, porous, and π-conjugated architectures interconnected through robust covalent bonds, have emerged as exceptional materials platforms owing to their modular synthetic design, precisely tunable pore geometries, and electron-rich backbones, conferring remarkable versatility across numerous applications [23–47]. COFs represent particularly promising candidates for photocatalytic applications [34–47], combining the advantages of organic materials—such as synthetic flexibility and sustainability—with the structural order and stability typically associated with inorganic systems. Their ability to integrate light-harvesting, charge separation, and catalytic functions within a single, customizable framework positions COFs as a cornerstone of next-generation photocatalytic technologies, with potential applications in sustainable energy production and environmental remediation.

Within this materials class, fluorine-functionalized COFs (F-COFs) have attracted attention for their distinctive properties [48–52], including strong electron-withdrawing effects, enhanced oxygen affinity, and superior chemical stability. These attributes have enabled their use in diverse fields, such as energy storage [53–55], adsorption and storage [51,56–58], electrocatalysis [59,60], and proton conduction [50]. However, only a limited number of F-COFs have been employed within the realm of photocatalysis [61–65]. Despite extensive investigations into key parameters such as photon absorption, energy level alignments, charge separation and transport, and water affinity to elucidate their photocatalytic behavior, the potential role of fluorine-induced modifications in proton transfer—an essential factor in photocatalytic proton-coupled electron-transfer (PCET) reactions—has been largely overlooked [66]. Given the fundamental involvement of protons in photocatalytic processes, addressing this gap is crucial for advancing the design and performance of COF-based photocatalysts.

In this study, we introduce a novel BF_2-bridged COF (C2-COF-BF2) synthesized via post-synthetic modification (PSM) of C2-COF using $BF_3 \cdot OEt_2$ (Scheme 1). This strategy aims to elucidate the effects of F incorporation on the physicochemical properties and photocatalytic performance of C2-COF-BF2, with a particular emphasis on proton transport dynamics. The incorporation of electron-deficient BF_2 moieties is expected to deliver dual functional benefits: first, creating a donor-acceptor (D-A) architecture to enhance light absorption, exciton dissociation, and charge transfer efficiency; and second, improving proton transport and fostering favorable interactions with protons. These synergistic enhancements are anticipated to significantly elevate the efficiency of photocatalytic PCET reactions, including the hydrogen evolution reaction (HER) and H_2O_2 production. As expected, C2-COF-BF_2 exhibits a HER rate exceeding that of its unmodified counterpart by more than threefold, alongside an over twofold increase in H_2O_2 production. These findings underscore the transformative potential of fluorine integration via PSM, presenting a promising strategy for optimizing charge carrier kinetics, facilitating proton transport, and advancing the design of COF-based photocatalysts for green energy applications.

2 Experimental

2.1 C2-COFs synthesis

4,4′,4′′,4′′′-(Pyrene-1,3,6,8-tetrayl)tetraaniline (PyTA) (14.2 mg, 0.025 mmol), 4,4′-(1,2-ethynediyl)bis[2-hydroxybenzal-

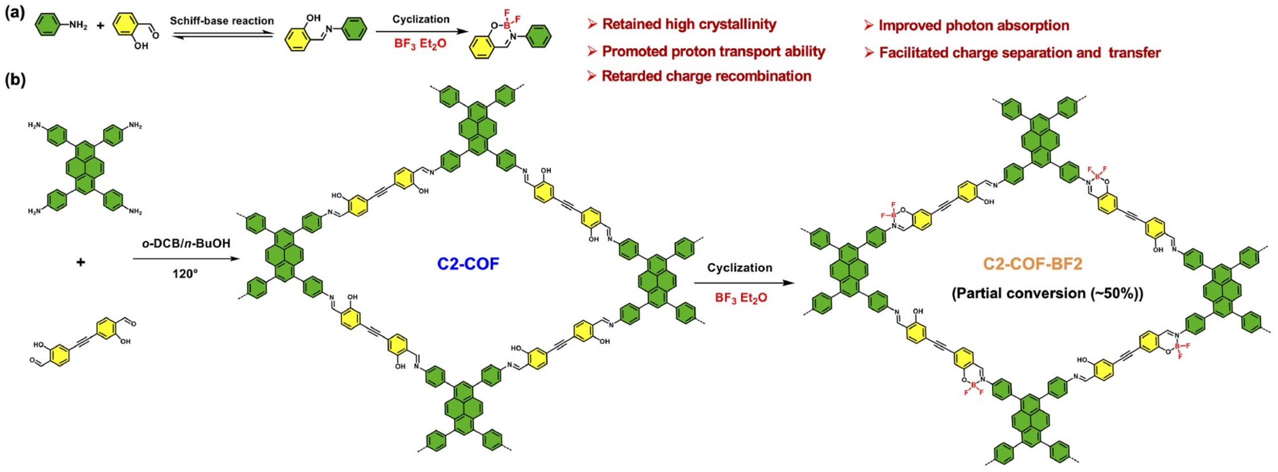

Scheme 1 (Color online) (a) Scheme representation of the formation of BF_2-functionalization molecules. (b) The synthetic routes for C2-COF-BF2 (Approximately 50% imine groups in C2-COF were converted to boranil linkages via cyclization. The structure shown represents a typical local environment).

dehyde] (M1) (13.3 mg, 0.05 mmol), *n*-BuOH (1 mL) and *o*-DCB (1 mL) were added to a 10 mL ampoule and sonicated for 2 min to form a homogeneous mixture. Subsequently, 6.0 M aqueous acetic acid (0.2 mL) was added to the dispersion. The ampoule was degassed using three freeze-pump-thaw cycles under liquid nitrogen and then flame-sealed. The sealed ampoule was heated at 120 °C for 3 d. After cooling to room temperature, the resulting yellow powder was collected by filtration and washed several times with acetone and tetrahydrofuran (THF), respectively. The precipitate was then subjected to Soxhlet extraction with THF for 24 h. Finally, the product was obtained by drying at 70 °C under reduced pressure for 2 h.

2.2 C2-COF-BF2 synthesis

Firstly, C2-COF (13 mg, 0.0125 mmol) was uniformly dispersed in 6 mL toluene in a 100 mL flask by sonication. Following the addition of $BF_3·OEt_2$ (7 μL, 0.05 mmol), the mixture was degassed and purged with Ar through 3 cycles of evacuation and refilling. The flask was then heated at 85 °C for 3 h. The resulting powder was collected by filtration and washed several times with methanol until the filtrate became colorless. Finally, the red precipitate was obtained by drying at 70 °C under vacuum.

3 Results and discussion

The construction of the targeted BF_2-bridged COF, C2-COF-BF2, involves a two-step process (Scheme 1b). Initially, a Schiff-base condensation reaction between PyTA and M1 yielded C2-COF. Subsequently, C2-COF was converted to C2-COF-BF2 via treatment with $BF_3·OEt_2$ (Details see the experimental section). Fourier transform infrared spectroscopy (FTIR) profiles (Figure 1a) revealed characteristic peaks at *ca*. 1620 cm^{-1}, attributed to C=N bonds in both COFs. Notably, the absence of aniline N–H stretching bands, typically observed between 3200 and 3400 cm^{-1}, and the carbonyl group (C=O) band at *ca*. 1660 cm^{-1}, was noted (Figure S1, Supporting Information online), confirming complete condensation in C2-COF. Meanwhile, the emergence of three new signals at *ca*. 1050, 1430, and 1530 cm^{-1} corresponds to B–N, B–O, and B–F within C2-COF-BF2, respectively, providing compelling evidence for successful BF_2 incorporation. Moreover, X-ray photoelectron spectroscopy (XPS) analysis of the N 1s region unraveled signals at 399.1 and 400.3 eV, ascribable to C=N and B–N bonds (Figure 1b), respectively. Additionally, the deconvoluted peaks in the O 1s XPS spectrum (Figure S2a) at 531.3 and 532.9 eV are assigned to B–O and C–O in C2-COF-BF2. Compared to C2-COF, noticeable signals were detected in the B 1s and F 1s spectra of C2-COF-BF2 (Figure S2b, c), indicating successful insertion of BF_2 moieties [61,67,68]. Quantitative XPS analysis showed that in C2-COF-BF2, the N content was approximately twice that of B, while the F content was roughly twice that of B (Table S1, Supporting Information online). The observed excess oxygen likely originates from atmospheric water or oxygen adsorbed on the sample surface. Based on this, we estimate the imine-to-boranil conversion rate at 46.5%. Complementary inductively coupled plasma mass spectrometry (ICP-MS) results indicated a boron content of *ca*. 1.55 wt% in C2-COF-BF2, suggesting an imine-to-boranil conversion efficiency of *ca*. 44.3%, aligning well with the XPS analysis. Furthermore, solid-state ^{13}C nuclear magnetic resonance spectrometry (^{13}C ssNMR) (Figure S3) confirmed the presence of alkynyl moieties (~90 ppm) and imine linkages (~159 ppm) in both COFs. Direct confirmation of boron incorporation in C2-COF-BF2 was obtained through solid-state ^{11}B NMR spectroscopy (Figure S4), which revealed a characteristic signal at −0.62 ppm, indicative of coordinated BF_2 units [69,70]. This finding confirms the successful bonding and anchoring of BF_2 moieties within the COF framework.

The crystalline structures of the COFs were assessed via powder X-ray diffraction (PXRD). C2-COF exhibited high crystallinity with prominent PXRD peaks at 2θ values of 3.10°, 6.06°, and 9.18° (Figure 1c), corresponding to the (100), (200), and (300) facets, respectively. Likewise, C2-COF-BF2 (Figure 1d) displayed analogous diffraction peaks and crystalline facets. Simulation with AA stacking for both COFs matched the experimental results well, signifying that both COFs adopt AA stacking modes (Figure 1c, d). Interestingly, C2-COF-BF2 maintained high crystallinity after PSM, even demonstrating a slight enhancement as evidenced by the narrower full-width-at-half-maximum (FWHM) of the (100) facet for C2-COF-BF2 (0.45°) compared to that of C2-COF (0.50°). This enhancement in crystallinity may be attributed to the Lewis acidic properties of $BF_3·OEt_2$, which promote reversible defect repair mechanisms within the imine-linked COF. During thermal treatment, the dynamic nature of imine linkages facilitates reversible bond formation and cleavage, enabling the incorporation of BF_2 moieties into the framework while simultaneously healing structural defects, thereby enhancing overall framework crystallinity. Additionally, the PSM with $BF_3·OEt_2$ introduces a step of reorganization in the COF framework. During this process, the initially less-ordered network may reorganize into a more thermodynamically stable crystalline state as the imine linkages are converted, thereby enhancing the crystallinity.

The high crystallinity of both COFs was further substantiated by the distinct lattice fringes observed in the transmission electron microscopy (TEM) images (Figures S5 and S6). Moreover, the high-angle annular dark field scanning transmission electron microscopy (HAADF STEM)

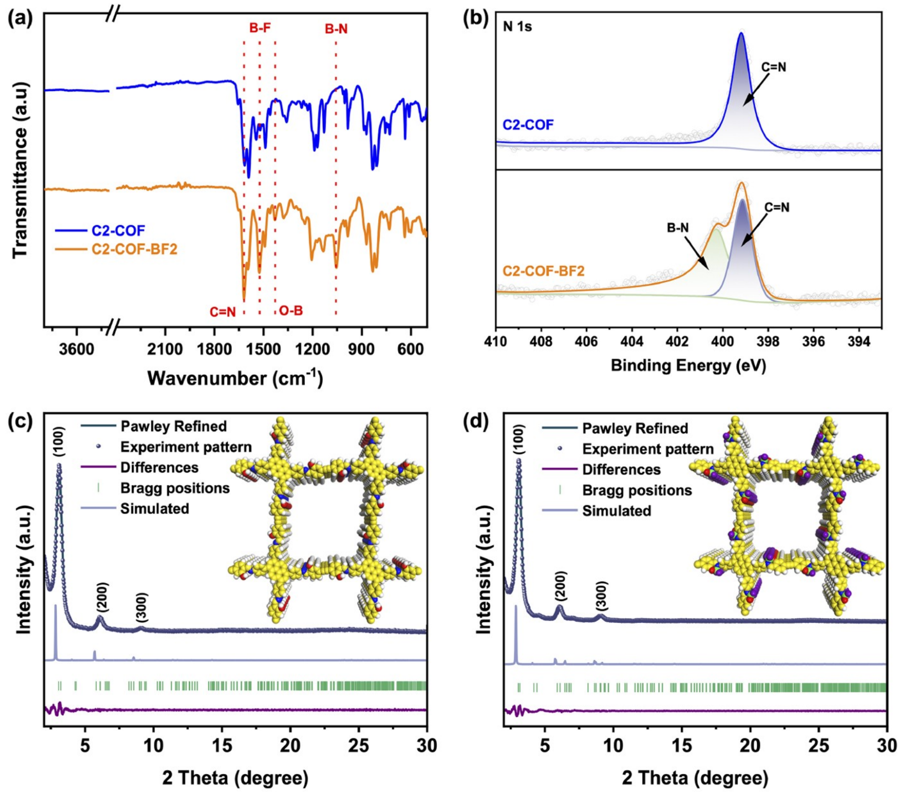

Figure 1 (Color online) (a) FTIR and (b) N 1s XPS spectra of C2-COF and C2-COF-BF2. PXRD patterns of (c) C2-COF and (d) C2-COF-BF2.

elemental mapping images revealed a uniform distribution of C, O, and N elements within C2-COF (Figure S5). Similarly, C, F, O, N, and B elements were found to be homogeneously spread throughout the framework of C2-COF-BF2 (Figure S6). These observations provide compelling evidence for the successful reaction between $BF_3{\cdot}OEt_2$ and imine motifs, resulting in the incorporation of BF_2 into the framework while preserving high crystallinity after PSM. The porosity of the as-prepared COFs was subsequently assessed via N_2 sorption isotherm at 77 K, yielding specific Brunauer-Emmett-Teller (BET) surface areas of 954 and 1201 $m^2\ g^{-1}$ for C2-COF and C2-COF-BF2, respectively (Figure S7). The counterintuitive increase in the BET specific surface area of C2-COF-BF2 may be ascribed to its enhanced crystallinity following PSM. Moreover, the PSM process likely facilitates the formation of more uniform and accessible nanopores, thereby augmenting the total surface area. Pore size distribution analyses unveiled the presence of one dominant mesopore with a diameter of *ca*. 2.79 and 2.59 nm for C2-COF and C2-COF-BF2, respectively (Figure S8). Furthermore, both COFs exhibited good thermal stability, with no significant weight loss observed up to 300 °C, as demonstrated by thermogravimetric analysis (TGA) (Figure S9).

As shown in the UV-vis diffuse reflectance spectroscopy (DRS) (Figure 2a), C2-COF-BF2 exhibited a broader light-harvesting range than C2-COF. This enhancement was related to the integration of the electron-deficient BF_2 moieties, which induced the D-A interactions. Their optical bandgaps could be calculated as 2.11 and 1.86 eV for C2-COF and C2-COF-BF2, respectively (Figure S10). Additionally, the flat-band potentials of C2-COF and C2-COF-BF2 derived from Mott-Schottky plots (Figure S11) were estimated to be −0.80 and −0.90 V, respectively. Accordingly, the energy level plot could be depicted (Figure 2b), clarifying that both COFs hold sufficient thermodynamic driving force for photocatalytic HER and H_2O_2 production.

To elucidate the impact of the BF_2-bridge on the charge separation and recombination kinetics, temperature-dependent photoluminescence (PL) spectra were conducted. Obviously, both COFs experienced the thermal quenching of their PL emission in the temperature range of 80–300 K (Figure 2c, d). By fitting the integrated PL intensities as a function of temperature employing the Arrhenius equation [12,71–74], the exciton binding energy (E_b) was determined as *ca*. 57 and 44 meV for C2-COF and C2-COF-BF2, respectively. Such a considerably low E_b value for C2-COF-BF2 is conducive to exciton dissociation, and thus facilitates photocatalysis [15,17,75,76]. Additionally, the steady-state PL emission intensity significantly attenuated from C2-COF to C2-COF-BF2 (Figure 2e), signifying suppressed charge recombination in the more structurally ordered C2-COF-BF2 [62,74,77,78]. Moreover, the average

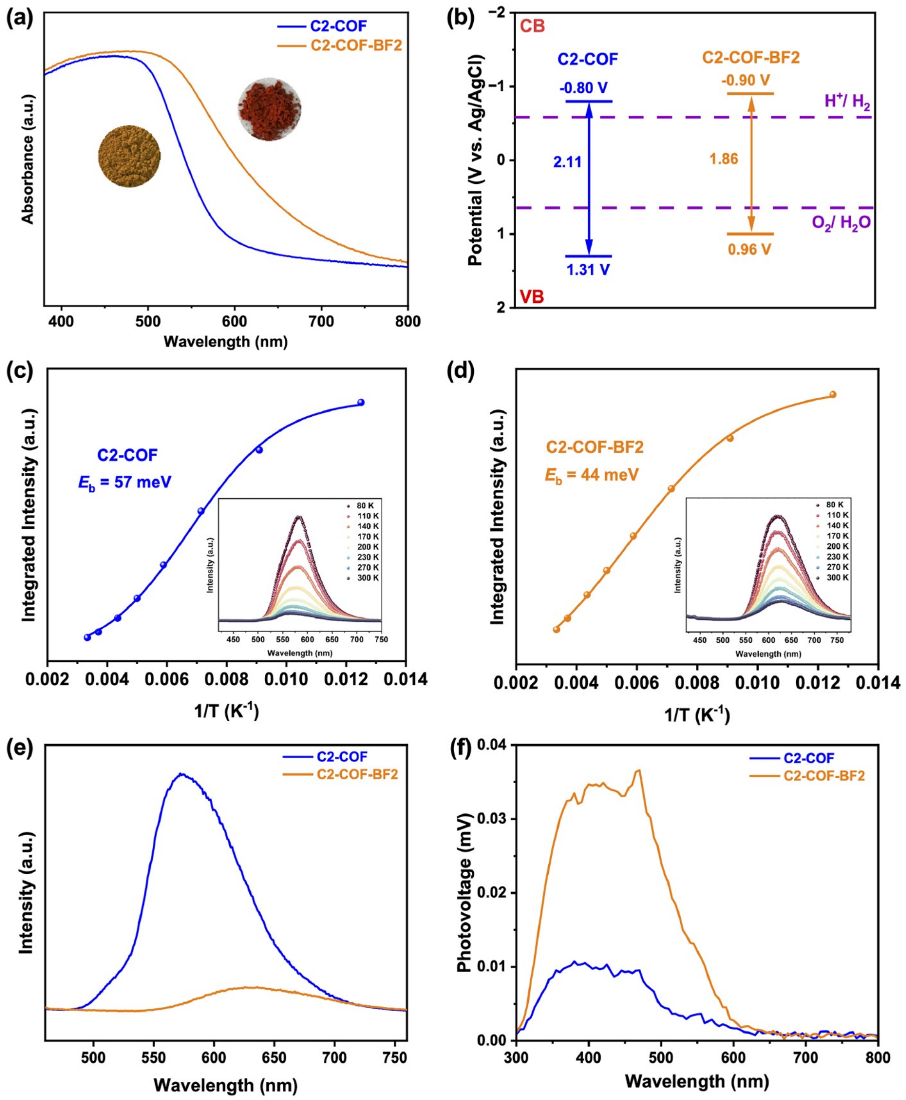

Figure 2 (Color online) (a) UV-vis DRS profiles (insets are the optical images of C2-COF and C2-COF-BF2). (b) The band diagrams of these COFs. Integrated PL emission intensity as a function of temperature from 80 to 300 K for (c) C2-COF and (d) C2-COF-BF2 (inset: temperature-dependent PL spectra). (e) The PL spectra results (λ_{ex} = 420 nm). (f) Steady-state surface photovoltage spectroscopy results.

lifetimes deduced from time-resolved PL spectra of the COFs were 0.9 and 1.12 ns for C2-COF and C2-COF-BF2, respectively (Figure S12). The longer lifetime of C2-COF-BF2 indicates more chances for photoinduced charges to be involved in the photocatalytic process, again highlighting the strategic introduction of BF_2 moieties to inhibit the recombination of photogenerated electron-hole pairs effectively. The observations suggest that BF_2-functionalization within C2-COF-BF2 could improve the separation efficiency of photogenerated charge upon light irradiation.

To obtain theoretical insights, we conducted density functional theory (DFT) calculations on the highest occupied molecule orbital (HOMO) and the lowest unoccupied molecule orbital (LUMO), as well as the Bader charges within these COFs. Comparatively, C2-COF-BF2 exhibits higher spatially separated delocalization of HOMO and LUMO (Figure S13) than those of C2-COF (Figure S14), demonstrating that the charge carrier recombination could be significantly suppressed and theoretically favored the charge separation, consistent with its lower E_b value. Bader charge analysis offers valuable insights into the assessment of charge transfer dynamics. Noticeably, the incorporation of BF_2 motifs into C2-COF effectively strengthened the electron-withdrawing ability of the acceptor (Figure S15). Consequently, the strong electron push-pull interactions would be generated for C2-COF-BF2, which could substantially reduce Coulombic electrostatic interactions and, in turn, lower the E_b. Therefore, the fluorinated molecular engineering strategy is a reliable protocol to expedite the charge migration kinetics.

Subsequently, we performed photoelectrochemical measurements to further analyze the charge migration behaviors.

As expected, C2-COF-BF2 manifested much stronger photocurrent response (Figure S16) and considerably smaller electrochemical impedance spectroscopy (EIS) radius upon dark or light irradiation (Figure S17). These results revealed that the C2-COF-BF2 features more efficient photoinduced carrier separation and migration. Moreover, C2-COF-BF2 also illustrated exceptional surface photovoltage spectroscopy (SPV) responses (Figure 2f) [79]. This result implies that an increased number of photoirradiation-induced carriers are generated and efficiently transferred from the interior to the surface of the C2-COF-BF2 during photocatalysis. These findings align with the conclusions derived from DFT and PL analyses, once again underscoring the pivotal role of the F-substitution in C2-COF-BF2 for the effective charge separation and migration.

Achieving desirable interactions between photocatalysts and substrates is critical for two-phase photocatalytic reactions, since good interaction between the active site and the proton, coupled with rapid proton transport in the pore channel, could effectively promote the efficiency of the photocatalytic reaction throughout the process. Given this, we then explored the correlation between proton transport within COF photocatalysts and photocatalytic activity. The impedance spectroscopy measurements were first conducted to assess proton conductivity performance at 98% relative humidity (RH) across a temperature range from 303 to 333 K. Notably, C2-COF exhibited substantial resistance to proton transport, particularly at 333 K, to the extent that a measurable value could not be obtained (Figure S18). In contrast, the conductivities of C2-COF-BF2 significantly enhanced to 6.258×10^{-8}, 7.489×10^{-8}, 9.090×10^{-8}, and 1.002×10^{-7} S cm^{-1}, respectively (Figure 3a and Figure S19). Subsequently, the activation energy (E_a) of proton transport was calculated to be 0.163 eV using Arrhenius plots (Figure 3b). With an E_a value below 0.4 eV, the proton conduction in C2-COF-BF2 was consistent with the Grötthuss hopping mechanism [50,52,80]. The explanation for the low activation energy suggested that the fluorinated networks have low resistance to proton transport, thereby making them conducive to proton conduction. The fluorine species in the pore wall were assembled into a dense hydrogen bonding network with the adsorbed water molecules, resulting in a Grötthuss mechanism for fluorinated C2-COF-BF2 that carried out proton conduction by hopping through a well-connected hydrogen bonding network. This mechanism is facilitated by the interactions between fluorine atoms and hydrogen atoms, which play a pivotal role in establishing the necessary conditions for efficient proton transport. Furthermore, the water contact angles (WCA) measurements of these samples were tested (Figure S20). Due to hydrogen bonding interaction given by the fluorine atoms, C2-COF-BF2 exhibited superior hydrophilicity in WCA (28.6°) to C2-COF (35.4°), demonstrating promoted interaction between the photocatalyst interface and water. Moreover, the inner pore environment of

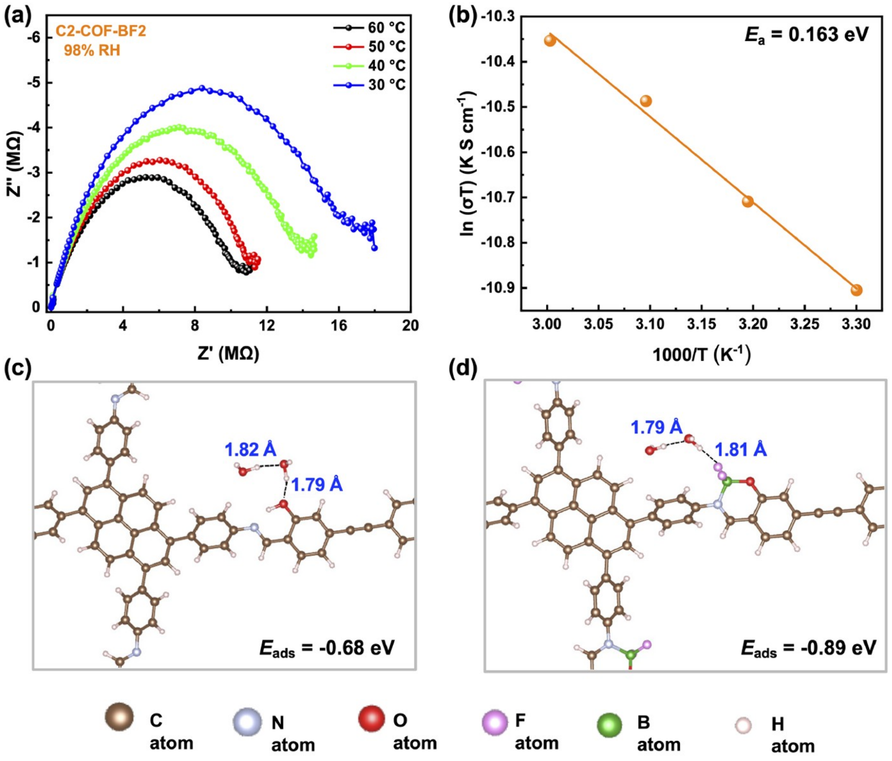

Figure 3 (Color online) (a) Nyquist plots of fluorinated C2-COF-BF2 at 98% RH. (b) Arrhenius plots for C2-COF-BF2. (c) C2-COF and (d) C2-COF-BF2 to calculate double water adsorption model structures.

these samples was further elucidated by water vapor uptake experiments at 298 K, where C2-COF-BF2 (0.66 g g^{-1}) showed a higher total water uptake than C2-COF (0.50 g g^{-1}) (Figure S21).

Notably, the DFT calculation outcomes also evidence that the BF_2 moieties in C2-COF-BF2 can offer sites to concentrate H_2O molecules and protons. Additionally, the adsorption energies for both single-H_2O and double-H_2O adsorption models on C2-COF-BF2 are stronger than those of the hydroxyl groups in C2-COF (Figure 3c, d and Figure S22). This endows that the BF_2 units could act as efficient proton extractors, potentially accelerating proton transfer and enhancing the kinetics of artificial photosynthesis. As a result, photogenerated carriers from the surfaces of the photocatalysts are able to carry out reduction reactions with the activated protons more promptly, thus apt to promote photocatalytic activity.

Based on the aforementioned experimental and theoretical results, photocatalytic HER in the presence of both COFs was initially conducted to verify our hypothesis. The HER performance of these COFs was evaluated using 3 wt% Pt as the co-catalyst. In contrast, C2-COF-BF2 presented a HER rate of 200 μmol h^{-1} (per 10 mg) (Figure 4a), over 3 times than that of C2-COF (65 μmol h^{-1}) (per 10 mg) under visible light illumination (λ > 420 nm) (experimental details see Supporting Information online). And an apparent quantum yield (AQY) of 8.78% at 450 nm, 8.53% at 500 nm, 1.77% at 600 nm and 0.67% at 650 nm were achieved (Figure 4b) for C2-COF-BF2. Notably, this value ($AQY_{450\ nm}$ = 8.78%) represents one of the highest reported values for COF photocatalysts to date (Table S3). Moreover, C2-COF-BF2 still maintained stable and continuous HER activity during a 6-h long-term experiment (Figure 4c) and 4-circles test within 16 h (Figure 4d). Notably, the recovered C2-COF-BF2 sample was re-characterized by FTIR (Figure S23) and PXRD (Figure S24), and no apparent change was observed, verifying its robust skeleton.

Furthermore, a secondary assay was conducted to evaluate

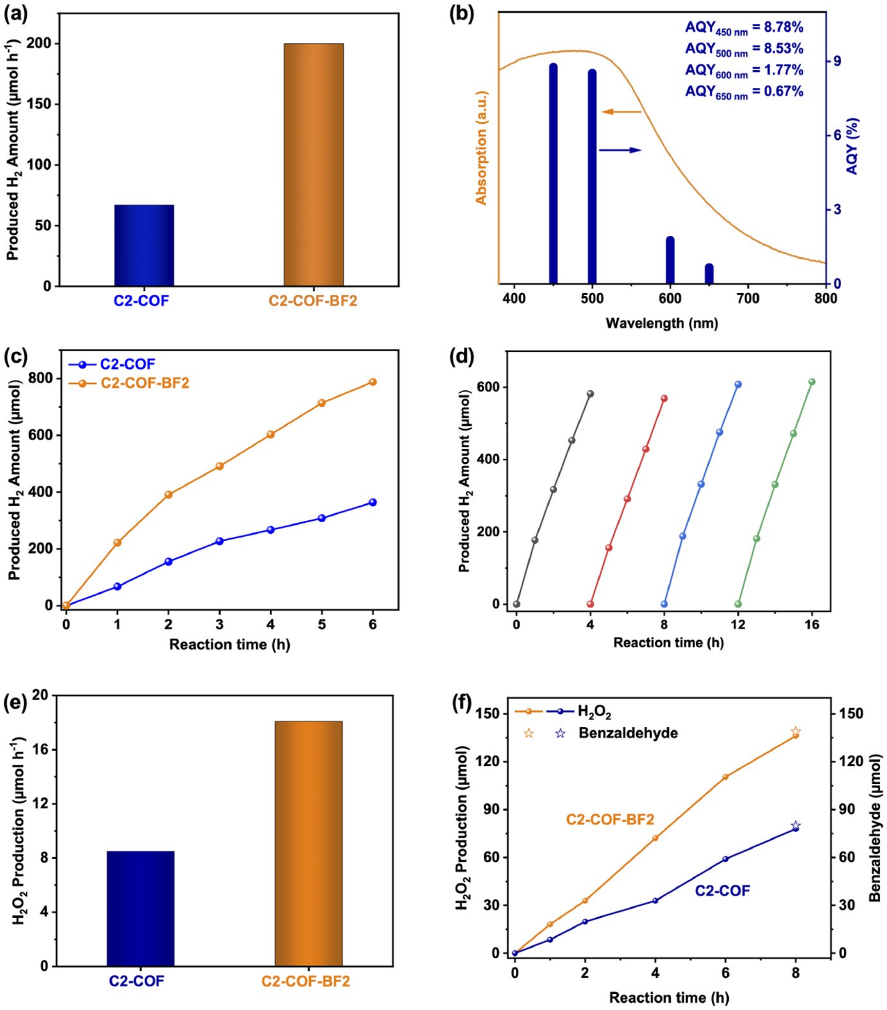

Figure 4 (Color online) Photocatalytic performances of C2-COF and C2-COF-BF2. (a) H_2 evolution rates (λ > 420 nm). (b) The wavelength-dependent AQYs of C2-COF-BF2. (c) Long-term H_2 evolution. (d) 4-Circles test for C2-COF-BF2. (e) H_2O_2 generation under visible-light irradiation. (f) Long-term H_2O_2 generation experiments.

the photocatalytic performance of these COFs, with particular emphasis on H_2O_2 production through the oxygen reduction reaction. Notably, C2-COF-BF2 achieved a H_2O_2 production rate (HPPR) of about 18.1 μmol h^{-1} (per 10 mg), significantly surpassing that of C2-COF, which was approximately 8.5 μmol h^{-1} (per 10 mg) (Figure 4e) in a biphasic system (experimental details see Supporting Information online). These COFs maintained stable and continuous HPPR activity throughout an 8-h prolonged experiment (Figure 4f). The H_2O_2 production efficiency of C2-COF-BF2 also surpasses that of some previously reported COF systems (Table S4). Concurrently, benzyl alcohol underwent oxidation to benzaldehyde at the oxidation end by photogenerated holes. The correlation between HPPR and HER performance underscores the efficacy of fluorine incorporation in these COFs. This modification significantly enhances charge separation and facilitates proton transport, which is crucial for efficient photocatalytic charge-induced reactions.

4 Conclusions

In summary, this study employs a PSM strategy to propose a BF_2-bridged COF (C2-COF-BF2) and systematically elucidates the role of BF_2-functionalization in enhancing photocatalytic PCET reductions, including HER and H_2O_2 production, underscoring the role of proton transport. The BF_2 motifs within C2-COF-BF2 function as efficient proton extractors, hypothesized to accelerate proton transport and thereby promote catalytic performance. Concurrently, the BF_2-insertion induces pronounced electron push-pull effects, which facilitate the charge separation and transfer kinetics, while impeding charge recombination. These synergistic enhancements contribute to the superior HER efficiency and HPPR of C2-COF-BF2, demonstrating a remarkable boost in photocatalytic activity. Both experimental and theoretical results provide compelling evidence supporting these findings. This approach offers valuable insights for the advancement of high-performance photocatalysts and paves the way for future innovations in sustainable energy applications.

Acknowledgements This work was supported by the National Natural Science Foundation of China (21972021, 22271281, 22325109, 22171263, 62227815, 91961115, 22494633, 22422508), the Natural Science Foundation of Fujian Province (2024J01238, 2022J06032, 2021J02017), the Scientific Research and Equipment Development Project of Chinese Academy of Sciences (YJKYQ20210024), the Fujian Science & Technology Innovation Laboratory for Optoelectronic Information of China (2021ZR101), the Self-deployment Project Research Program of Haixi Institutes, Chinese Academy of Sciences (CXZX-2022-GH09, CXZX-2023-GS03, CXZX-2022-JQ03), the Key Research Project of Chinese Academy of Sciences (KGFZD-145-25-21), the Strategic Priority Research Program of Chinese Academy of Sciences (XDB1170000), and the 111 Project (D16008).

Conflict of interest The authors declare no conflict of interest.

Supporting information The supporting information is available online at http://chem.scichina.com and http://link.springer.com/journal/11426. The supporting materials are published as submitted, without typesetting or editing. The responsibility for scientific accuracy and content remains entirely with the authors.

1 Dai C, Liu B. *Energy Environ Sci*, 2020, 13: 24–52
2 Tan D, Zhuang R, Chen R, Ban M, Feng W, Xu F, Chen X, Wang Q. *Adv Funct Mater*, 2024, 34: 2311655
3 Song H, Luo S, Huang H, Deng B, Ye J. *ACS Energy Lett*, 2022, 7: 1043–1065
4 Wang X, Maeda K, Thomas A, Takanabe K, Xin G, Carlsson JM, Domen K, Antonietti M. *Nat Mater*, 2009, 8: 76–80
5 Zhang J S, Wang B, Wang X C. *Acta Physico-Chim Sin*, 2013, 29: 1865–1876
6 Li G, Xie Z, Chai S, Chen X, Wang X. *Appl Catal B-Environ*, 2021, 283: 119637
7 Liu M, Zhang G, Liang X, Pan Z, Zheng D, Wang S, Yu Z, Hou Y, Wang X. *Angew Chem Int Ed*, 2023, 62: e202304694
8 Liu F, Deng J, Su B, Peng KS, Liu K, Lin X, Hung SF, Chen X, Lu XF, Fang Y, Zhang G, Wang S. *ACS Catal*, 2025, 15: 1018–1026
9 Lan ZA, Ren W, Chen X, Zhang Y, Wang X. *Appl Catal B-Environ*, 2019, 245: 596–603
10 Li G, Xie Z, Wang Q, Chen X, Zhang Y, Wang X. *Chem Eur J*, 2021, 27: 939–943
11 Xie Z, Wang W, Ke X, Cai X, Chen X, Wang S, Lin W, Wang X. *Appl Catal B-Environ*, 2023, 325: 122312
12 Luo Z, Chen X, Hu Y, Chen X, Lin W, Wu X, Wang X. *Angew Chem Int Ed*, 2023, 62: e202304875
13 Li C, Xu H, Xiong H, Xia S, Peng X, Xu F, Chen X. *Adv Funct Mater*, 2024, 34: 2405539
14 Sachs M, Sprick RS, Pearce D, Hillman SAJ, Monti A, Guilbert AAY, Brownbill NJ, Dimitrov S, Shi X, Blanc F, Zwijnenburg MA, Nelson J, Durrant JR, Cooper AI. *Nat Commun*, 2018, 9: 4968
15 Lan Z, Zhang G, Chen X, Zhang Y, Zhang KAI, Wang X. *Angew Chem Int Ed*, 2019, 58: 10236–10240
16 Woods DJ, Hillman SAJ, Pearce D, Wilbraham L, Flagg LQ, Duffy W, McCulloch I, Durrant JR, Guilbert AAY, Zwijnenburg MA, Sprick RS, Nelson J, Cooper AI. *Energy Environ Sci*, 2020, 13: 1843–1855
17 Lan Z, Wu M, Fang Z, Chi X, Chen X, Zhang Y, Wang X. *Angew Chem Int Ed*, 2021, 60: 16355–16359
18 Wang X, Chen L, Chong SY, Little MA, Wu Y, Zhu WH, Clowes R, Yan Y, Zwijnenburg MA, Sprick RS, Cooper AI. *Nat Chem*, 2018, 10: 1180–1189
19 Chai S, Chen X, Zhang X, Fang Y, Sprick RS, Chen X. *Environ Sci-Nano*, 2022, 9: 2464–2469
20 Lu M, Zhang S, Yang M, Liu Y, Liao J, Huang P, Zhang M, Li S, Su Z, Lan Y. *Angew Chem Int Ed*, 2023, 62: e202307632
21 Chen D, Chen W, Wu Y, Wang L, Wu X, Xu H, Chen L. *Angew Chem Int Ed*, 2023, 62: e202217479
22 Xie Z, Chen X, Wang W, Ke X, Zhang X, Wang S, Wu X, Yu JC, Wang X. *Angew Chem Int Ed*, 2024, 63: e202410179
23 Cote AP, Benin AI, Ockwig NW, O'Keeffe M, Matzger AJ, Yaghi OM. *Science*, 2005, 310: 1166–1170
24 Hao Q, Tao Y, Ding X, Yang Y, Feng J, Wang RL, Chen XM, Chen GL, Li X, OuYang H, Hu XL, Tian J, Han BH, Zhu G, Wang W, Zhang F, Tan B, Li ZT, Wang D, Wan LJ. *Sci China Chem*, 2023, 66: 620–682
25 Xu F, Yang S, Chen X, Liu Q, Li H, Wang H, Wei B, Jiang D. *Chem Sci*, 2019, 10: 6001–6006
26 Yu H, Zhou P, Chen X. *Adv Funct Mater*, 2023, 33: 2308336
27 Zhou P, Yu H, Li Y, Yu H, Chen Q, Chen X. *J Polym Sci*, 2024, 62: 1536–1553
28 Zhou P, Li Y, Zeng T, Chee MY, Huang Y, Yu Z, Yu H, Yu H, Huang W, Chen X. *Angew Chem Int Ed*, 2024, 63: e202402911

29 Zhou PK, Huang Y, Yu Z, Zhang C, Chen Q, Li Y, Lin C, Chen X. *Sci China Chem*, 2025, 68: 3230–3237

30 Hao Q, Ren XR, Chen Y, Zhao C, Xu J, Wang D, Liu H. *Nat Commun*, 2023, 14: 578

31 Hu J, Zhang J, Lin Z, Xie L, Liao S, Chen X. *Chem Mater*, 2022, 34: 5249–5257

32 Weng W, Guo J. *J Am Chem Soc*, 2024, 146: 13201–13209

33 Han X, Jiang C, Hou B, Liu Y, Cui Y. *J Am Chem Soc*, 2024, 146: 6733–6743

34 Nagai A, Chen X, Feng X, Ding X, Guo Z, Jiang D. *Angew Chem Int Ed*, 2013, 52: 3770–3774

35 Yin HQ, Zhang ZM, Lu TB. *Acc Chem Res*, 2023, 56: 2676–2687

36 Peng Y, Guo G, Guo S, Kong L, Lu T, Zhang Z. *Angew Chem Int Ed*, 2021, 60: 22062–22069

37 Wang S, Sun Q, Chen W, Tang Y, Aguila B, Pan Y, Zheng A, Yang Z, Wojtas L, Ma S, Xiao FS. *Matter*, 2020, 2: 416–427

38 Luo Z, Zhu S, Xue H, Yang W, Zhang F, Xu F, Lin W, Wang H, Chen X. *Angew Chem Int Ed*, 2025, 64: e202420217

39 Wang Y, Zhang F, Huang F, Dong X, Zeng B, Gu XK, Lang X. *Appl Catal B-Environ Energy*, 2024, 354: 124103

40 Yu H, Zhang F, Chen Q, Zhou P, Xing W, Wang S, Zhang G, Jiang Y, Chen X. *Angew Chem Int Ed*, 2024, 63: e202402297

41 Liu N, Xie S, Huang Y, Lu J, Shi H, Xu S, Zhang G, Chen X. *Adv Energy Mater*, 2024, 14: 2402395

42 Chi X, Zhang Z, Li M, Jiao Y, Li X, Meng F, Xue B, Wu D, Zhang F. *Angew Chem Int Ed*, 2025, 64: e202418895

43 Cheng J, Wu Y, Zhang W, Zhang J, Wang L, Zhou M, Fan F, Wu X, Xu H. *Adv Mater*, 2024, 36: 2305313

44 Yu H, Zhang X, Chen Q, Zhou PK, Xu F, Wang H, Chen X. *Chem Res Chin Univ*, 2024, doi: 10.1007/s40242-024-4213-3

45 Liu J, Tuo C, Xiao W, Qi M, Yusran Y, Wang Z, Li H, Guo C, Song J, Qiu S, Xu Y, Fang Q. *Angew Chem Int Ed*, 2025, 64: e202416240

46 Xie S, Liu R, Liu N, Xu H, Chen X, Wang X, Jiang D. *Angew Chem Int Ed*, 2025, 64: e202416771

47 Li J, Zhou J, Wang X, Guo C, Li R, Zhuang H, Feng W, Hua Y, Lan Y. *Angew Chem Int Ed*, 2024, 63: e202411721

48 Chen X, Addicoat M, Irle S, Nagai A, Jiang D. *J Am Chem Soc*, 2013, 135: 546–549

49 Martínez-Abadía M, Mateo-Alonso A. *Adv Mater*, 2020, 32: e2002366

50 Wu X, Hong Y, Xu B, Nishiyama Y, Jiang W, Zhu J, Zhang G, Kitagawa S, Horike S. *J Am Chem Soc*, 2020, 142: 14357–14364

51 Liu Y, Li W, Yuan C, Jia L, Liu Y, Huang A, Cui Y. *Angew Chem Int Ed*, 2022, 61: e202113348

52 Guan L, Guo Z, Zhou Q, Zhang J, Cheng C, Wang S, Zhu X, Dai S, Jin S. *Nat Commun*, 2023, 14: 8114

53 Lee J, Lim H, Park J, Kim M, Jung J, Kim J, Kim I. *Adv Energy Mater*, 2023, 13: 2300442

54 Cao Q, Wan L, Xu Z, Kuang W, Liu H, Zhang X, Zhang W, Lu Y, Yao Y, Wang B, Liu K. *Adv Mater*, 2023, 35: 2210550

55 Zhang K, Li X, Ma L, Chen F, Chen Z, Yuan Y, Zhao Y, Yang J, Liu J, Xie K, Loh KP. *ACS Nano*, 2023, 17: 2901–2911

56 Zhao Y, Sui Z, Chang Z, Wang S, Liang Y, Liu X, Feng L, Chen Q, Wang N. *J Mater Chem A*, 2020, 8: 25156–25164

57 Zheng Q, Liu J, Wu Y, Ji Y, Lin Z. *Anal Chem*, 2022, 94: 18067–18073

58 Shi Y, Xu R, Wang S, Zheng J, Zhu F, Hu Q, Huang J, Ouyang G. *Adv Sci*, 2023, 10: 2302925

59 Martínez-Fernández M, Martínez-Periñán E, de la Peña Ruigómez A, Cabrera-Trujillo JJ, Navarro JAR, Aguilar-Galindo F, Rodríguez-San-Miguel D, Ramos M, Vismara R, Zamora F, Lorenzo E, Segura JL. *Angew Chem Int Ed*, 2023, 62: e202313940

60 Jiménez-Duro M, Martínez-Periñán E, Martínez-Fernández M, Martínez JI, Lorenzo E, Segura JL. *Small*, 2024, 20: 2402082

61 Borse RA, Tan Y, Lin J, Zhou E, Hui Y, Yuan D, Wang Y. *Angew Chem Int Ed*, 2024, 63: e202318136

62 Chen W, Wang L, Mo D, He F, Wen Z, Wu X, Xu H, Chen L. *Angew Chem Int Ed*, 2020, 59: 16902–16909

63 Zhao Z, Zheng Y, Wang C, Zhang S, Song J, Li Y, Ma S, Cheng P, Zhang Z, Chen Y. *ACS Catal*, 2021, 11: 2098–2107

64 Liu Y, Li L, Tan H, Ye N, Gu Y, Zhao S, Zhang S, Luo M, Guo S. *J Am Chem Soc*, 2023, 145: 19877–19884

65 Wang M, Wang Z, Shan M, Wang J, Qiu Z, Song J, Li Z. *Chem Mater*, 2023, 35: 5368–5377

66 Lin Y, Zou J, Wu X, Tong S, Niu Q, He S, Luo S, Yang C. *Nano Lett*, 2024, 24: 6302–6311

67 Peng Y, Li L, Zhu C, Chen B, Zhao M, Zhang Z, Lai Z, Zhang X, Tan C, Han Y, Zhu Y, Zhang H. *J Am Chem Soc*, 2020, 142: 13162–13169

68 Yan X, Lyu S, Xu X, Chen W, Shang P, Yang Z, Zhang G, Chen W, Wang Y, Chen L. *Angew Chem Int Ed*, 2022, 61: e202201900

69 Alvarez-Quesada A, Trujillo-González DE, Jiménez-Halla JOC, Báez JE, Ramos-Ortiz G, González-García G. *J Mol Struct*, 2025, 1325: 140980

70 Provinciali G, Consoli NA, Caliandro R, Mangini V, Barba L, Giannini C, Tuci G, Giambastiani G, Lelli M, Rossin A. *J Phys Chem C*, 2025, 129: 6094–6108

71 Xie Z, Yang X, Zhang P, Ke X, Yuan X, Zhai L, Wang W, Qin N, Cui CX, Qu L, Chen X. *Chin J Catal*, 2023, 47: 171–180

72 Xu H, Xia S, Li C, Li Y, Xing W, Jiang Y, Chen X. *Angew Chem Int Ed*, 2024, 63: e202405476

73 Gao X, Yuan J, Wei P, Dong J, Chang L, Huang Z, Zheng H, Liu J, Jia J, Luan T, Zhou B, Yu H, Peng C. *ACS Catal*, 2023, 14: 533–546

74 Qian Y, Han Y, Zhang X, Yang G, Zhang G, Jiang HL. *Nat Commun*, 2023, 14: 3083

75 Fu G, Yang D, Xu S, Li S, Zhao Y, Yang H, Wu D, Petkov PS, Lan ZA, Wang X, Zhang T. *J Am Chem Soc*, 2024, 146: 1318–1325

76 Yan H, Peng Y, Huang Y, Shen M, Wei X, Zou W, Tong Q, Zhou N, Xu J, Zhang Y, Ye Y, Ouyang G. *Adv Mater*, 2024, 36: 2311535

77 Lin Z, Yu X, Zhao Z, Ding N, Wang C, Hu K, Zhu Y, Guo J. *Nat Commun*, 2025, 16: 1940

78 Sun T, Liang Y, Xu Y. *Angew Chem Int Ed*, 2022, 61: e202113926

79 Li S, Hou LB, Zhang L, Chen L, Lin Y, wang D, Xie T. *J Mater Chem A*, 2015, 3: 17820–17826

80 Chen J, An B, Chen Y, Han X, Mei Q, He M, Cheng Y, Vitorica-Yrezabal IJ, Natrajan LS, Lee D, Ramirez-Cuesta AJ, Yang S, Schröder M. *J Am Chem Soc*, 2023, 145: 19225–19231